Terahertz pulsed imaging of low velocity impact damage in woven fiber composite laminates

Pascal Pomarède, Nada Miqoi, David Christophe, David S. Citrin, Fodil Meraghni, Alexandre Locquet

Terahertz pulsed imaging of low velocity impact damage in woven fiber composite laminates

Authors: P. Pomarède[1,2], N. Miqoi[1,2], D. Christophe[2], D.S. Citrin[1,3], F. Meraghni[2] and A. Locquet[1,3]

Affiliations:

1: Georgia Tech-CNRS IRL2958
Georgia Tech-Europe, 2 Rue Marconi, 57070 Metz, France
e-mail: ppomarede@georgiatech-metz.fr, alocquet@georgiatech-metz.fr, david.citrin@ece.gatech.edu

2: Arts et Métiers Institute of Technology, CNRS, Université de Lorraine, LEM3-UMR 7239 CNRS
4 rue Augustin Fresnel, 57078 Metz, France
e-mail: fodil.meraghni@ensam.eu

3: School of Electrical and Computer Engineering,
Georgia Institute of Technology, Atlanta, GA, 30332-0250, USA
e-mail: alocquet@georgiatech-metz.fr, david.citrin@ece.gatech.edu

Abstract

Recently, terahertz pulse imaging has been used extensively to characterize internal defects in various electrically insulating materials. In this work, terahertz pulse imaging is used to identify the damage induced by low-velocity impact on woven glass-fiber reinforced polyamide laminates. Several impact energies are considered to study the damage initiation and propagation. The permanent indentation, known to be a relevant damage indicator, is extracted from the terahertz results and validated through comparison with profilometry. Further, the criticality of the damage, in terms of the number of composite plies in which the cracks propagate, can be clearly determined from terahertz imaging. These observations are validated through X-ray tomographic observations and analysis. Finally, a strong connection is established between the evolution of the permanent indentation and the appearance, and criticality, of the low-velocity impact-induced damage. These observations suggest that terahertz imaging is a reliable technique for the nondestructive assessment of impact damage in glass fiber composites.

Keywords: Woven fiber reinforced composite, Non-Destructive Evaluation, Terahertz pulse imaging, Damage detection, Low-velocity impact

1. Introduction

Fiber reinforced composites are being increasingly used in applications requiring load-bearing components [1, 2]. This is mostly due to their excellent weight/strength ratio, durability, and low cost motivating their extensive use in the aerospace and automotive industries. In addition, another important aspect of these materials is their high corrosion and weather resistance [3]; they are increasingly used to repair or replace corroded structures, such as pipelines [4, 5]. Under thermomechanical loading, composite laminates, however, can suffer from various damage types such as matrix cracking, interface debonding, fiber breakage, and delamination, notably when the thickness increases [6–9]. One common loading configuration to which they are often exposed, but is challenging to assess, is low-velocity impact as the damage may not be prominent upon casual inspection. Indeed, this type of impact can induce internal damage in composites that may not be visually detected [8], and such damage is thus referred to as barely visible impact damage (BVID), and corresponds to a threshold commonly adopted in the nondestructive

evaluation (NDE) domain [10]. Even though this damage may not appear visually to be severe, there may be more serious internal damage, and its accumulation can lead to the materials progressive degradation that can have a catastrophic detrimental effect on the lifetime and in-service response of the composite [11–13].

For low-velocity, but high-momentum, impact, the impactor can leave a permanent indentation (PI) mark (imprint) on the structure. However, this trace is typically difficult to detect by standard visual inspection during standard maintenance and/or structural health assessment. The depth and volume of this PI is known to be function of the impact energy and, as a consequence, of the internal damage induced by the impact [14, 15]. In addition, it can indicate the initiation of damage even in the BVID range [16]. Therefore, it is a useful indicator to assess damage criticality.

There is an imperative need to develop innovative NDE methods aimed at detecting and quantifying the criticality of these damage mechanisms with two objectives in mind, namely (i) measurement of the PI marks on impacted surface even in the BVID domain and (ii) detection and quantification of the damage mechanisms induced inside of the composite. Several NDE techniques have already been investigated including X-ray tomography [17, 18], thermography [19], and ultrasound [15, 20, 21]. Each method has its pros and cons, and needs to be carefully carried out based on cost, damage size, safety, efficiency, and portability [22–24]. High resolution can be achieved with X-ray tomography, but it is an inspection approach that can be long and is ionizing thus presenting health risks to human operators. Thermographic inspection tends to be faster, but with a lower resolution. Ultrasound, by contrast, exhibits a time of inspection and a resolution that is in between the other two methods overall. Of course, it depends on the specific method used, as even two ultrasound-based methods can have their resolution, time of inspection, etc. varying significantly.

Nevertheless, terahertz (THz) imaging has emerged as a promising technique for damage detection and evaluation in composites. The THz portion of the electromagnetic spectrum extends by convention from 100 GHz to 10 THz and lies between the microwave and infrared ranges. It provides a noninvasive, noncontact, and nonionizing method to characterize electrically insulating materials. It can offer a better resolution than ultrasound in imaging defects in depth [25] and does not carry health risks as is the case for X-ray tomography [26]. Further, commercial THz imaging systems are compact and robust, and available at rapidly falling cost, which makes them good candidates for in-service inspection. THz-based techniques have been used on composite laminates to measure, *e.g.*, fiber orientation [27, 28], to characterize the constituents of the composite [29], to detect forced delamination [30], fatigue-induced damage, [31] and heat damage [32]. In addition, previous works [25, 33, 34] have investigated damage induced by low-velocity impact; however, either the existing studies only imaged surface damage, or only one impact energy was investigated. In order to develop a practical tool for on-site industrial use, it is important to consider a larger range of impact energies and perform a detailed study of the induced internal damage to confirm the validity of PI as an indicator of the damage criticality.

In this work, samples of woven glass-fiber composite laminates impacted at various low-impact energies are investigated. Seven impact energies are considered, all in the BVID domain, and the samples are examined by THz imaging. The PI, which increases with impact energy, and can be employed as a tool to assess impact criticality, is firstly measured by THz imaging of the surface and the values obtained compared with other techniques. The next step is to perform THz imaging on the impacted samples, yielding both surface and depth information, and characterizing the criticality of the induced damage. These samples are also investigated and analyzed by X-ray tomography to interpret and validate the THz observations and to characterize the dependence of the damage area on the impact energy. Finally, a link is established between the evolution of the PI and the damage that can be detected internally in the sample. Our results

highlight the capability of THz imaging for the shop-floor and in-service maintenance of composite material-based components.

2. Materials and methods

2.1 Materials and impact tests

The material used in this investigation is a semi-crystalline co-polyamide 66/6 reinforced with 3 layers (for a total thickness of 1.53 mm) of 2/2 twill woven glass fibers oriented 0°/90° (balanced reinforcement) manufactured by DuPont. A detailed structural characterization of this material can be found in recent works [15, 20]. These materials are extensively employed in automotive components, for instance in the side-intrusion beams, due to their higher impact-energy absorption than metallic or thermoset polymer-based composite materials. The composite, with a thickness of 1.53 mm, has a fibre weight ratio of 63 % corresponding to a fiber volume fraction of 43 %. Table 1 summarizes the elastic properties and the ultimate strength and strain of the studied composite material.

Fiber volume content	Density	$E_{0°}$(GPa) warp direction	$E_{90°}$ (GPa) weft direction	σ_{UTS}(MPa) warp direction	ε_{UTS} (%) warp direction
0.43	1.78	17.7	18.1	303	1.9

Table 1: Mechanical characteristics of the studied woven glass fabric-PA66-6 composite.

The impact tests are performed with a drop-weight impact machine (Figure 1). A 16-mm-diameter hemispherical impactor of 1.02 kg is used. The system consists of a piezoelectric load sensor and two laser displacement sensors, as well as a data acquisition system. Eight samples of 100 x 150 x 1.53 mm^3, plates clamped at both ends during the impact tests, are tested. The impactor height is varied in order to obtain 7 impact energy levels, namely 8.5, 13.1, 13.7, 14.2, 15.7, 18.1, 23, and 25 J. An undamaged sample is also retained as a control.

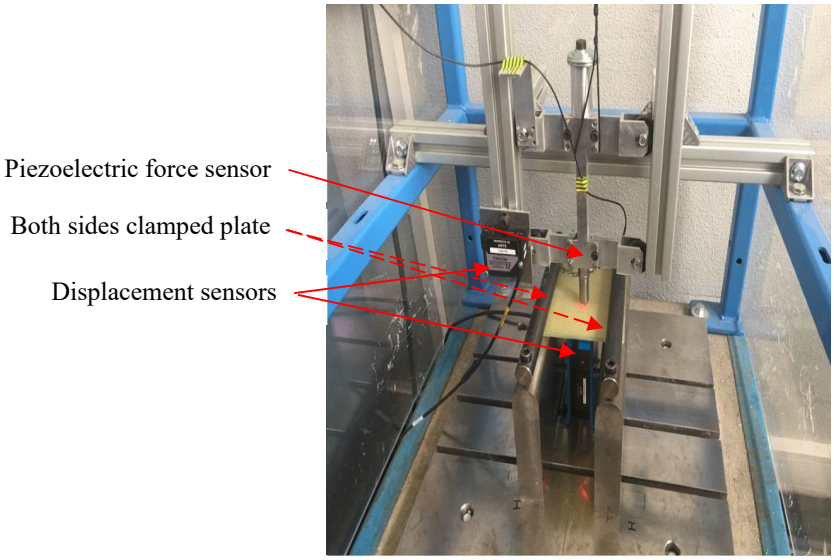

Figure 1: Drop-weight impact machine. A piezoelectric force sensor and a laser displacement sensor monitor the striker contact force and its displacement. Another laser displacement sensor monitors the sample deformation during the impact [15].

2.2 THz imaging and signal processing

For all the THz measurements described in this paper, a THz time-domain spectroscopy (THz-TDS) system (TeraView Ltd. TPS Spectra 3000) is employed in reflection mode. The acquisitions were done at a room temperature of 25°C. The system is shown schematically in Figure 2. The apparatus produces THz pulses with a bandwidth from 60 GHz to 3 THz and the signal is averaged over 5 shots per time delay per pixel. The recorded THz waveforms have 2048 data points with a time sampling of 0.023 ps. An *xy* scanner is used to image a 60 x 60 mm *xy* region with a 0.2 mm spatial step. The transverse resolution at 1 THz is ~400 µm due to the choice of the numerical aperture of the THz optics that provide a depth of focus the well exceeds the sample thickness. The acquired data is also used later for the internal damage investigation.

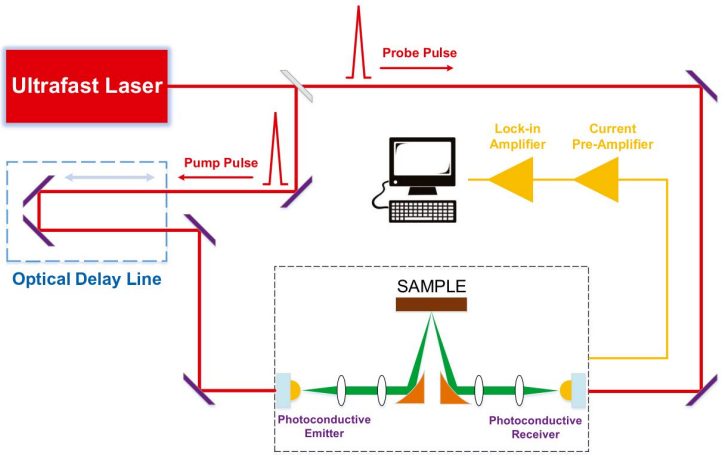

Figure 2: Schematic diagram of THz time-domain spectroscopy (THz-TDS) system in reflection mode [35].

After recording the data, the signals are processed for reducing the noise by applying a 0.2 THz high-pass filter and wavelet denoising. The wavelet transform convolves a signal with a low- and high-pass filter along the temporal axis for every chosen number of decomposition level. It gives approximate coefficient vectors and detail coefficients for each level. The coefficients with small values can be considered as noise and removed from the signal by soft thresholding and reconstruction of the signal. More details about the procedure can be found in [35]. In this work, symlet 4 wavelets are used with a maximum level of 7. The B- and C-scans are spatially averaged within a five-pixels radius.

The effect of the impact on the creation of a permanent indentation mark, and its measurement will be discussed in next section. The analysis of the induced internal damage will be addressed in a following section.

3. Permanent indentation

After an impact test, the impactor leaves a permanent indentation (PI) mark on the impacted surface. The depth of the PI is known to increase with the impact energy, and it reflects the level of the induced internal damage as illustrated in Figure 3. In this section, the PI depth is measured using two techniques: optical profilometry that is used to provide reference measurements and THz imaging in reflection. For both methods, the PI location is first identified and then the maximum depth of the PI is measured accordingly.

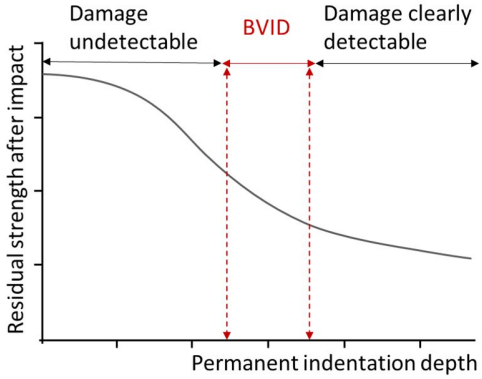

Figure 3: Schematic representation of the evolution of the residual strength after impact as a function of the measured PI on composites materials. The visual detectability range is also indicated from undetectable to detectable.

3.1 Optical profilometry

For the optical profilometry measurements, a LEICA DCM3D is employed. A magnification of 5x is chosen with a scan size of 27 x 20.23 mm^2. This gives a lateral resolution of 0.94 µm and a vertical resolution smaller than 150 nm. All the seven impacted samples are scanned and the surface-texture maps obtained are post-processed using Leica Maps software. A filter is applied to elevate the surface around the impacted area, to separate the roughness of the sample from the waviness due to the impact. An example of surface texture obtained before and after applying the filter is given in Figure 4. The PI depth is then extracted as the deepest value. The evolution of the PI depth with impact energy is plotted in Figure 5. From this result, three main stages can be identified. First, the PI increases slightly until a value around 25 µm depth

corresponding to an impact energy level of 14.2 J. A stabilization of the PI depth is observed until 18.1 J of impact energy. The PI depth finally further increases significantly reaching a value of 144 µm.

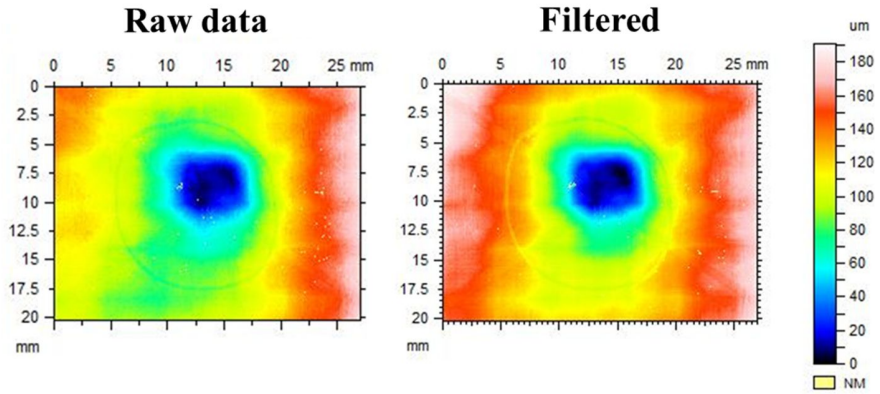

Figure 4: Surface texture of a sample, after an impact of 25 J, obtained using the optical profilometry, before (left) and after (right) applying a filter.

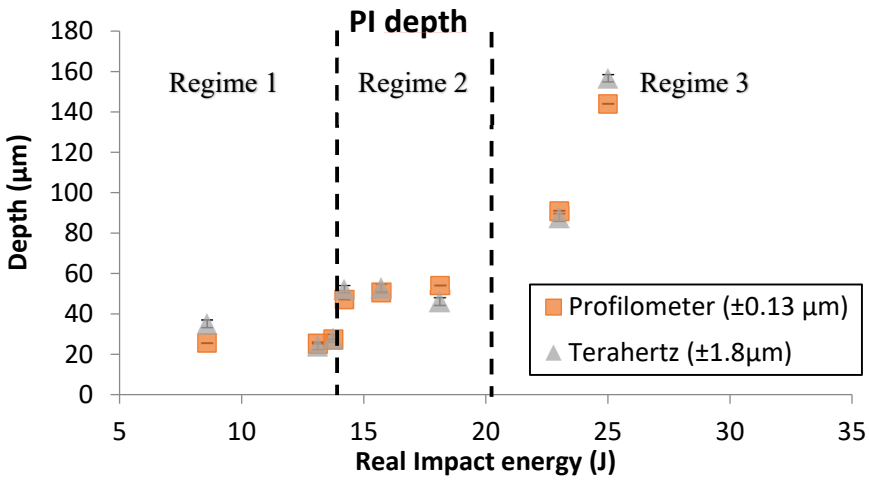

Figure 5: Comparison of PI depth obtained by optical profilometry and THz imaging. The two methods are in substantial agreement and exhibit three impact-energy regimes. The first shows an increase of PI depth with impact energy, then a stabilization regime, and at high impact energy, a regime with a large increase of the PI depth with impact energy.

3.2 THz measurement

An example of recorded signals after processing is shown in Figure 6A. To extract the PI, the time of arrival of the first positive peak is measured as illustrated in Figure 6C around the coordinates [12 ps 18 mm] of the PI. Visualizing the impacted area from the C-scan of the top surface can help to narrow the investigated area (see Figure 6B). The contrast mechanism chosen is the amplitude of the first positive peak in the reflected signal, which has the highest amplitude due to the large refractive-index mismatch between air and the composite matrix. Thus, the C-scan shown using this contrast mechanism provides information about the sample-surface morphology. An example of the procedure to extract the time of arrival from the THz data is depicted in Figure 7. First, a linear-regression algorithm is used on the first peaks at the ends

of the surface (not taking into account the PI) to obtain the position of the nonimpacted sample surface, represented as a red continuous line in the figure. Then, the time of arrival differences, between all the positive first peaks of the entire sample surface and the nonimpacted surface, are calculated. An example of this time difference, for a given first peak, is represented as a dashed red line in the figure. The black line links this first peak to the point on the nonimpacted sample surface sharing the same x coordinate. This time difference is calculated as the sine of the angle between the nonimpacted sample surface and this black line θ times the length of the black line. Finally, all PI depths of each B-scan are compared to determine the largest indentation depth. All the PI measured are shown in Figure 5. Good agreement with the results from optical profilometry is observed, establishing the suitability of the THz imaging as a resolved measurement of the PI.

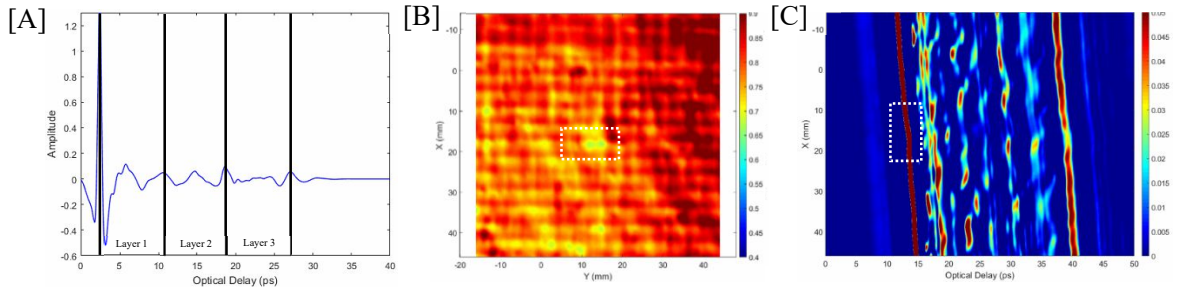

Figure 6: [A] Example of THz signal after a 0.2 THz high pass filter and wavelet denoising. Several echoes corresponding to the interfaces are visible and are indicated by the vertical black lines. The three layers of the sample are indicated on the figure. [B] C-scan based on the amplitude of the first echo (~2.45 ps) after spatial averaging. The impacted area is clearly visible in the center. [C] B-scan near PI visible at the coordinates t = 12 ps and y = 18 mm. All figures were obtained from the sample impacted at 18.1 J. The PI location is indicated by dotted boxes.

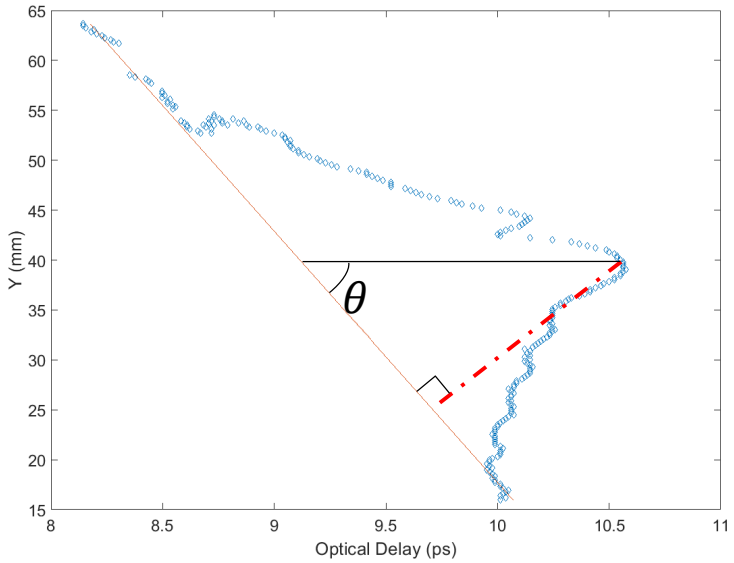

Figure 7 : Linear PI-depth regression plot on a B-scan at x = -15.5 mm of a sample impacted at 25 J with example of PI depth. The solid red line is the nonimpacted sample surface obtained by regression. The red dotted line is the arrival time corresponding to the PI depth for a given point we wish to measure. The black line links this point to the continous black line, with the y-coordinate constant. The sine of the angle θ times the length of the black line gives the expected time of arrival. This calculation needs to be carried out at all points and all x-slices to find the largest PI depth.

4. Internal damage

In addition to the PI, the impact loading can create other damage types in a composite laminate. Thin plates are known to bend during impact [36]. Damage initiates on side opposite the impact and then propagates inside the sample. In the following, the damage mechanisms and the criticality of the generated damage are investigated and compare it with the PI depth investigated in the previous section. The damage is visualized from THz B-scans at selected locations. The impacted samples are first investigated by X-ray tomography, providing a higher-resolution comparison and a reference for the THz results. X-ray tomography is carried out with an EasyTom (Nano) device developed by RX solutions. The voxel size resolution is set to 12 µm which corresponds to the size of the fiber diameter and the recorded data are post processed using the AVIZO software.

~~The same signal processing method, described in Sec. 3.2, is used in this part for THz data~~. When examining a typical B-scan (Figure 6C), evidence of individual plies from reflections (echoes) due to refractive-index mismatch between the matrix and the fibers determined by the Fresnel coefficients. In addition, there is a 4.1 mm long periodic increase of the amplitude along each layer for a fixed optical delay. This is due to the 2/2 twill weave architecture of the woven-fabric layer as this length scale corresponds to the yarns' diameter. Indeed, the intersection between the 0° and 90° yarns will create a local refractive-index mismatch between the matrix and the fabric reinforcement bringing about a local increase of the amplitude. It means that even in the absence of PI or internal damage, the composite microstructure induces a complex THz B-scan that can be difficult to interpret and analyze. Consequently, analyzing the internal damage in this material requires a thorough examination with respect to a reference configuration of an undamaged sample.

With the exception of creating a PI on the impacted surface, the lowest impact energies do not induce discernable damage within the samples; nothing is visible either in the THz or X-ray tomography results. In increasing the impact energy, the first damage mechanism is matrix cracking on the surface opposite the impacted side observed after an impact energy of 14.2 J. This is visible in X-ray tomography but also visually on the sample (see Figure 8A). In the THz B-scan (see Figure 8C), matrix cracking appears as a local decrease of the amplitude of the echo corresponding to the matrix/air interface (near 37 ps). This cracking is also visible in the THz C-scan of the nonimpacted surface in Figure 8B. This can be explained by THz scattering due to the enhancement of surface inhomogeneity ensuing matrix and fiber crack propagation to the surface [37]. When analyzing the image of the interior plies, no additional damage is immediately evident.

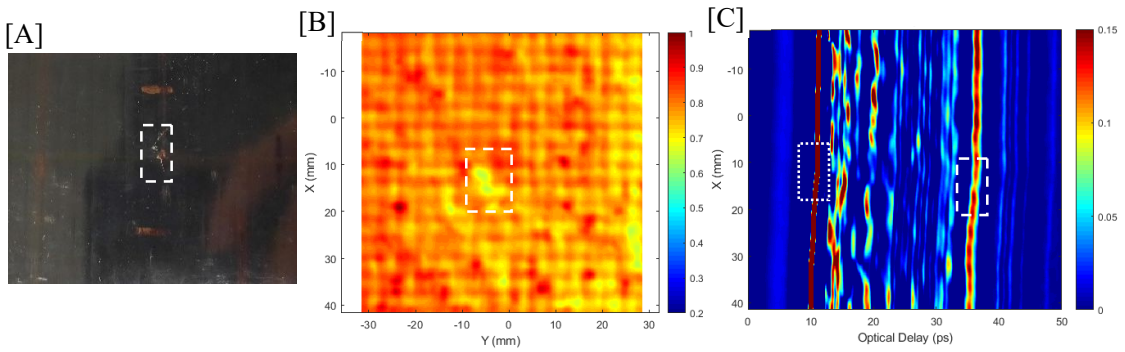

Figure 8: Analysis of the sample impacted at 14.2 J. [A] Photograph of the nonimpacted surface showing matrix cracking within dashed box. [B] THz C-scan of the non-impacted surface of the sample. Matrix cracking is visible as a decrease of the amplitude. [C] THz B-scans of the sample. The damage mechanisms are indicated as follows: *dotted box*: PI, *dashed box*: cracking of bottom surface.

When the impact energy reaches 18.1 J, additional damage mechanisms come into play, the accumulation of which leads to the initiation of delamination. The latter is clearly visible in the third ply of the sample by X-ray tomography in Figure 9B. Indeed, this delamination originates in matrix cracking on the nonimpacted surface and is created by an increase of bending, leading to the propagation of the cracks within the material. The same location is analyzed using THz B-scans in Figure 9A. Similar to Figure 8, the PI on the top surface and the matrix cracks on the bottom are observed. Moreover, in the third layer, there is a local increase of the amplitude around 35 ps and $x = 20$ mm. This increase of the amplitude is located just below the matrix cracks indicating that it results from pseudo-delamination in the third layer of the sample. Indeed, the delamination creates a new air/matrix interface at this location, which results in a new echo in the reflected signal [37]. A typical B-scan of a nondamaged sample is shown in Figure 9C for comparison. As already mentioned, the interpretation of the results can be arduous due to the interaction of the THz beams with the structure of the woven fabric creating amplitude variations along a layer. Nevertheless, these observations highlight and assess the capability of THz imaging to detect internal damage even in a composite material exhibiting complex microstructure such a woven fiber composite laminate.

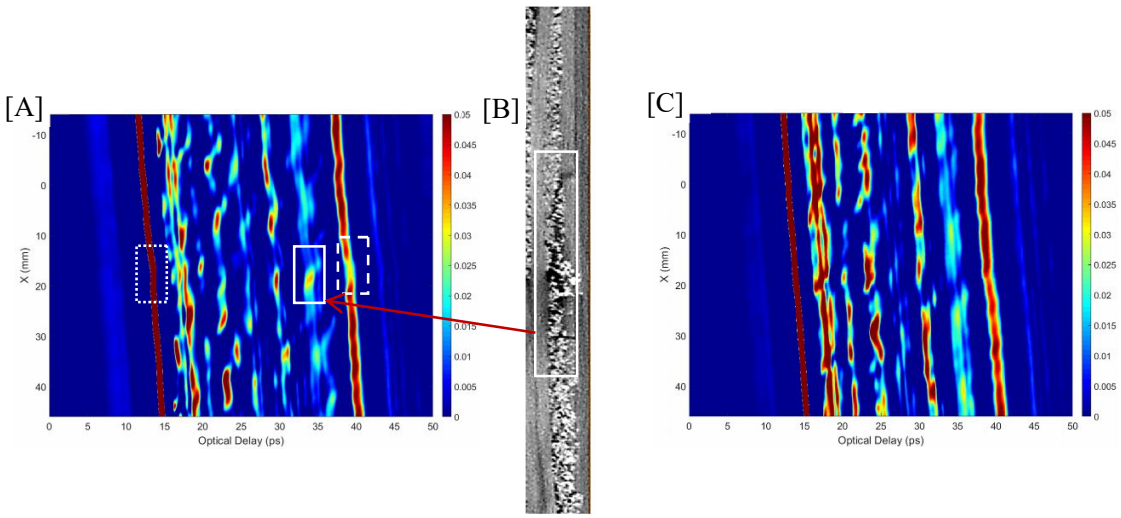

Figure 9: Analysis of the sample impacted at 18.1 J. [A] THz B-scan at impact location. [B] X-ray tomography image of the third layer near the impact location with a visible delamination. [C] Typical THz B-scan representation of an undamaged sample for comparison. Various damage types are visible: dotted box: permanent indentation (PI), dashed box: cracks on the bottom surface and continuous line box: delamination in the third layer.

For an even larger impact energy of 23 J, a crack network starting from the non-impacted side propagates until the second layer of the plate. This is visible in X-ray tomography and boxed in white in Figure 10A and C and. It is the only crack network detected from the X-ray investigation and is located near the impacted region, as expected. This highlights the fact that the damage mechanisms are strongly concentrated near this region.

The propagation of the damage area is also detected from the THz images (see Figure 10B). The impact region is clearly visible around 17 ps and $x = 20$ mm. The small delamination near the nonimpacted side appears as a local increase of the amplitude (white dashed box). Similar local increases of the amplitude in the second layer (continuous-line box) are noticed. As the impact energy is important, the deformation of

layer is also visible inside of the material and not only in the surface. It appears as ripples in the white box in the Figure 10B.

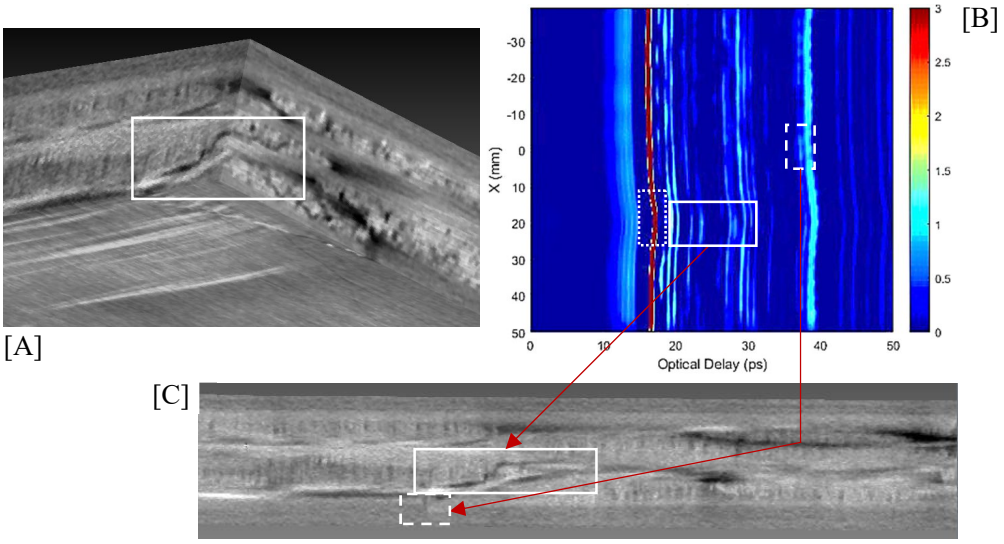

Figure 10: Analysis of the sample impacted at 23 J. [A] X-ray tomography image of the interior of the sample with the propagation of a crack to the second ply. [B] THz B-scan near the impacted region. [C] X-ray tomography image near the impacted region. Multiple damage types are visible: dotted box: Permanent Indentation (PI), dashed box: cracks on the bottom surface, and continuous line box: delamination in the third layer.

Finally, for an impact energy of 25 J, the damage propagates further and reaches the third layer, as seen in X-ray tomography in Figure 11B and in Figure 12B and C. In these figures, matrix cracking and delamination are visible in various layers and are connected with each other, indicating again matrix cracking, originating from the non-impacted surface, and propagating toward the impacted surface. This is especially visible in Figure 12B. In addition to the PI, matrix cracks appear on the impacted surface and are especially visible in Figure 12B and C.

From the THz B-scans, delamination can also be detected between various layers. They appear as several local increases of the amplitude, highlighted by the continuous-line boxes, in Figure 11A and C and in Figure 12A. As the damage path does not propagate within a single cross-section of the material, THz B-scans at x = -15.5 mm and -17.28 mm, are plotted in Figure 11A and C, respectively. The internal damage area follows the same path as in the X-ray tomography of Figure 11B. Matrix cracking on the nonimpacted surface again appears as an amplitude decrease (near 34 ps). Matrix cracking on the impacted surface also occurs; however, as the first echo is large in amplitude, it appears saturated in the figures. Similar observations can be made from the THz B-scans of Figure 12. The matrix cracks and the delamination propagating from the nonimpacted surface to the other are detected, as well as the matrix cracks near the two outer surfaces of the sample.

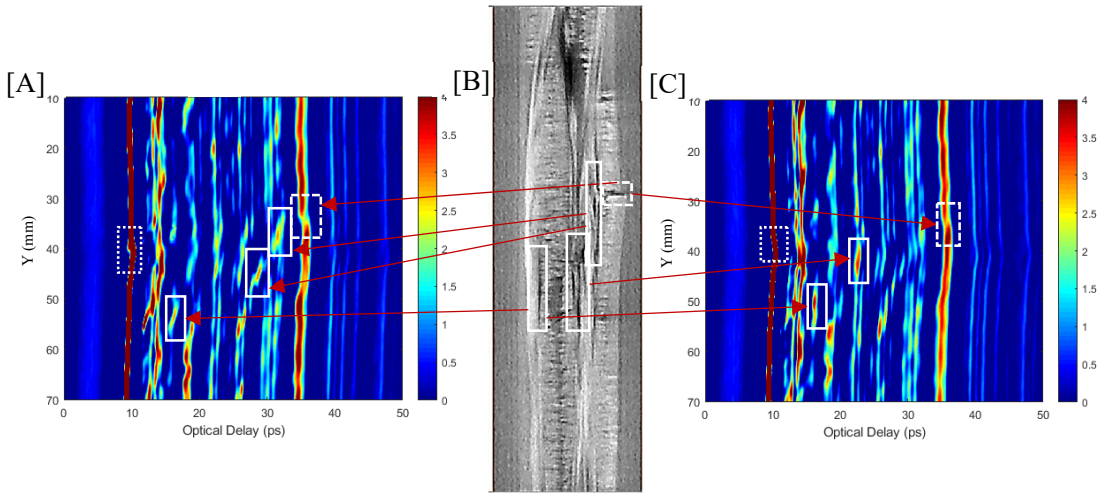

Figure 11: Analysis of sample impacted at 25 J. THz B-scan near PI at [A] x = -15.5 mm and [C] x = -17.28 mm. Some delaminations are more visible in one or the other B-scans. [B] X-ray tomography image of the damage mechanisms near the PI. Delamination and matrix cracking propagate in all layers. Various damage types are visible: *dotted box*: permanent indentation (PI) + matrix cracks, *dashed box*: cracks on the bottom surface, and *continuous line box*: delamination.

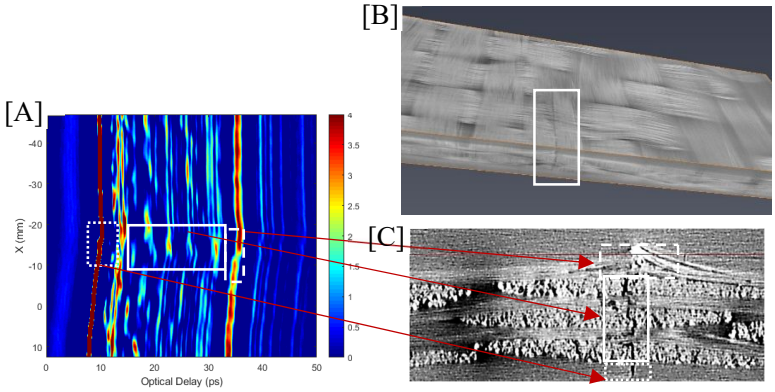

Figure 12: Analysis of the sample impacted at 25 J. [A] THz B-scan at near the impacted region. X-ray tomography image of the matrix cracks running from the non-impacted surface to the other in 3D [B] and in a longitudinal slice [C]. Various damage types are visible: *dotted box*: permanent indentation (PI) + matrix cracks, *dashed box*: cracks on the bottom surface, and *continuous line box*: delamination.

5. Discussion

With THz imaging, the damage initiation and propagation can be observed, which allow to determine the following scenario of the progressive material degradation. All the chosen impact energies lead to the generation of a PI on the impacted surface. From 8.5 to 13.7 J, no additional damage has been generated. When reaching 14.2 J, matrix cracking is visible on the non-impacted surface, a significant increase of the PI depth is also noted. As expected, the size of the matrix cracks increases with impact energy. In this impact-energy range, PI depth also gradually increases. For an energy level about 18.1 J, delamination mechanism is initiated between the surface plies on the non-impacted side. The PI depth is in a stabilization regime until 18.1 J. After this energy level, the PI depth increases drastically with the impact energy, which is consistent with the increase of the observed damage area. Indeed, the crack network propagates deeper

into the sample, along the second (at 23 J) and then the third layer (at 25 J). This damage scenario and the associated impact-energy level, as well as the corresponding PI depths, are summarized in Figure 13.

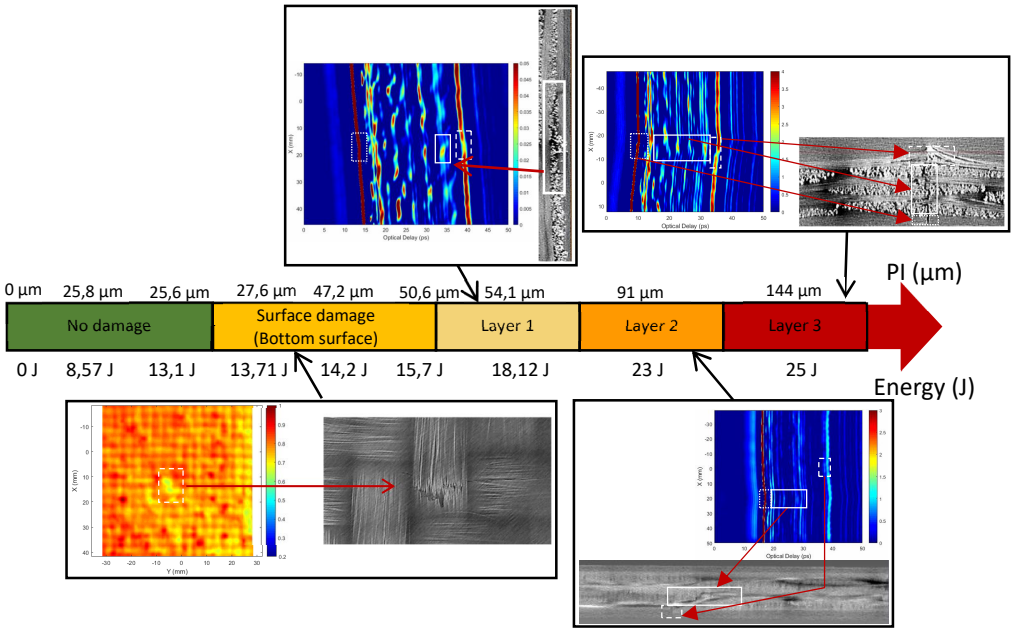

Figure 13: Summary of the proposed damage scenario for the studied material when undergo impact event. The propagation of damage through the sample are indicated. The impact energy as well as the PI depth are also given

6. Conclusion

In this work, we have studied the capability of THz imaging to simultaneously detect and quantify the PI on the surface of an impacted sample and the induced damage generated in a woven-fabric composite laminate. Several impact energy levels, close to the BVID range, have been considered to investigate more realistic induced defects. Damage mechanisms such as matrix cracking, delamination and cracks networks, have been observed in the THz images. These observations have been verified by means of X-ray tomography. The PI depth has been also measured, as it increases with the impact energy, the obtained values agree with resolved optical profilometry measurements. This makes the measurement of the PI depth, with THz, a possible way for assessing the overall criticality of the induced damage.

The investigated composite material with a complex reinforcement architecture remains, however, difficult to analyze due to its microstructure as well as the subsequent interaction with the THz radiation. This could make image interpretation difficult for human operators in shop-floor or field-inspection applications, especially for relatively low damage levels. Defect identification by means of THz imaging may in the future be facilitated by machine-learning approaches.

AKNOWLEDGEMENTS

A.L. and D.S.C. acknowledge the financial support of the Région Grand Est. A.L and D.S.C. thank the CPER SusChemProc. A.L, D.S.C., P.P, and F.M acknowledge financial support from Institut Carnot ARTS. D.R acknowledge the support of the Chair in Photonics.

References

1. (2020) Global Composites Market – Industry Trends and Forecast to 2027. In: DataBridgeMarketResearch.com. https://www.databridgemarketresearch.com/reports/global-composites-market
2. Davies P (2016) Behavior of marine composite materials under deep submergence. Mar Appl Adv Fibre-Reinforced Compos 125–145. https://doi.org/10.1016/B978-1-78242-250-1.00006-5
3. Sloan J (2020) The markets: Industrial (2021). In: CompositeWorlds.com. https://www.compositesworld.com/articles/the-markets-industrial-2021
4. Lee YJ, Lee JR, Ihn JB (2018) Composite repair patch evaluation using pulse-echo laser ultrasonic correlation mapping method. Compos Struct 204:395–401. https://doi.org/10.1016/J.COMPSTRUCT.2018.07.124
5. Liu F, Zhou Z, Liu S, et al (2020) Evaluation of carbon fiber composite repairs using asymmetric-frequency ultrasound waves. Compos Part B Eng 181:107534. https://doi.org/10.1016/J.COMPOSITESB.2019.107534
6. Karayaka M, Kurath P (1994) Deformation and Failure Behavior of Woven Composite Laminates. J Eng Mater Techology 116:222–232
7. Montesano J, Fawaz Z, Bougherara H (2015) Non-destructive assessment of the fatigue strength and damage progression of satin woven fiber reinforced polymer matrix composites. Compos Part B Eng 71:122–130. https://doi.org/10.1016/j.compositesb.2014.11.005
8. Agrawal S, Singh KK, Sarkar P-K (2013) Impact damage on fibre-reinforced polymer matrix composite – A review. J Compos Mater 48:317–332. https://doi.org/10.1177/0021998312472217
9. Gul S, Tabrizi IE, Okan BS, et al (2021) An experimental investigation on damage mechanisms of thick hybrid composite structures under flexural loading using multi-instrument measurements. Aerosp Sci Technol 117:106921. https://doi.org/10.1016/J.AST.2021.106921
10. Sierakowski RL, Newaz GM (1995) Damage tolerance in advanced composites, First edit
11. Kara M, Muhammed K (2017) Effects of the number of fatigue cycles on the impact behavior of glass fi ber / epoxy composite tubes. Compos Part B Eng 123:55–63. https://doi.org/10.1016/j.compositesb.2017.04.021
12. Atas C, Sayman O (2008) An overall view on impact response of woven fabric composite plates. Compos Struct 82:336–345. https://doi.org/10.1016/j.compstruct.2007.01.014
13. Marguères P, Meraghni F (2013) Damage induced anisotropy and stiffness reduction evaluation in composite materials using ultrasonic wave transmission. Compos Part A Appl Sci Manuf 45:134–144
14. Shah SZH, Karuppanan S, Megat-yuso PSM, Sajid Z (2019) Impact resistance and damage tolerance of fiber reinforced composites : A review. 217:100–121. https://doi.org/10.1016/j.compstruct.2019.03.021
15. Miqoi N, Pomarède P, Meraghni F, et al (2020) Detection and evaluation of barely visible impact damage in woven glass fabric reinforced polyamide 6.6/6 composites using ultrasonic imaging , X-

ray tomography and optical profilometry. Int J Damage Mech 30:1–26. https://doi.org/10.1177/1056789520957703

16. Hongkarnjanakul N (2013) Modélisation numérique pour la tolérance aux dommages d'impact sur stratifié composite : de l'impact à la résistance résiduelle en compression

17. Holmes J, Sommacal S, Stachurski Z, et al (2022) Digital image and volume correlation with X-ray micro-computed tomography for deformation and damage characterisation of woven fibre-reinforced composites. Compos Struct 279:114775. https://doi.org/10.1016/J.COMPSTRUCT.2021.114775

18. Madra A, Hajj N El, Benzeggagh ML (2014) X-ray microtomography applications for quantitative and qualitative analysis of porosity in woven glass fiber reinforced thermoplastic. Compos Sci Technol 95:50–58. https://doi.org/10.1016/j.compscitech.2014.02.009

19. Maier A, Schmidt R, Oswald-Tranta B, Schledjewski R (2014) Non-Destructive Thermography Analysis of Impact Damage on Large-Scale CFRP Automotive Parts. Materials (Basel) 7:413–429. https://doi.org/10.3390/ma7010413

20. Pomarède P, Meraghni F, Peltier L, et al (2018) Damage Evaluation in Woven Glass Reinforced Polyamide 6 . 6 / 6 Composites Using Ultrasound Phase-Shift Analysis and X-ray Tomography. J Nondestruct Eval 37:. https://doi.org/10.1007/s10921-018-0467-3

21. Su Z, Ye L, Lu Y (2006) Guided Lamb waves for identification of damage in composite structures : A review. J Sound Vib 295:753–780. https://doi.org/10.1016/j.jsv.2006.01.020

22. Gholizadeh S (2016) A review of non-destructive testing methods of composite materials. In: Procedia Structural Integrity. Elsevier B.V., pp 50–57

23. Garnier C, Pastor M-L, Eyma F, Lorrain B (2011) The detection of aeronautical defects in situ on composite structures using Non Destructive Testing. Compos Struct 93:1328–1336

24. Howell PA (2020) Nondestructive Evaluation (NDE) Methods and Capabilities Handbook. Langley Research Center, Hampton, Virginia February

25. Dong J, Locquet A, Declercq NF, Citrin DS (2016) Polarization-resolved terahertz imaging of intra- and inter-laminar damages in hybrid fi ber-reinforced composite laminate subject to low-velocity impact. Compos Part B Eng 92:167–174. https://doi.org/10.1016/j.compositesb.2016.02.016

26. Wilmink GJ, Grundt JE (2011) Current state of research on biological effects of terahertz radiation. J Infrared, Millimeter, Terahertz Waves 32:1074–1122. https://doi.org/10.1007/S10762-011-9794-5/FIGURES/8

27. Jördens C, Scheller M, Wietzke S, et al (2010) Terahertz spectroscopy to study the orientation of glass fibres in reinforced plastics. Compos Sci Technol 70:472–477. https://doi.org/10.1016/j.compscitech.2009.11.022

28. Calvo-de la Rosa J, Pomarède P, Antonik P, et al (2023) Determination of the process-induced microstructure of woven glass fabric reinforced polyamide 6.6/6 composite using terahertz pulsed imaging. NDT E Int 102799. https://doi.org/10.1016/j.ndteint.2023.102799

29. Naftaly M, Miles RE (2007) Terahertz time-domain spectroscopy for material characterization. Proc IEEE 95:1658–1665. https://doi.org/10.1109/JPROC.2007.898835

30. Dong J, Kim B, Locquet A, et al (2015) Nondestructive evaluation of forced delamination in glass fiber-reinforced composites by terahertz and ultrasonic waves. Compos Part B Eng 79:667–675.

https://doi.org/10.1016/j.compositesb.2015.05.028

31. Lopato P, Chady T (2014) Terahertz examination of fatigue loaded composite materials. Int J Appl Electromagn Mech 45:613–619. https://doi.org/10.3233/JAE-141884

32. Radzieński M, Mieloszyk M, Rahani EK, et al (2015) Heat induced damage detection in composite materials by terahertz radiation. https://doi.org/101117/122084144 9438:402–411. https://doi.org/10.1117/12.2084144

33. Destic F, Bouvet C (2016) Impact damages detection on composite materials by THz imaging. Case Stud Nondestruct Test Eval 6:53–62

34. Malinowski PH, Ostachowicz WM, Touchard F, et al (2018) Study of plant fibre composites with damage induced by laser and mechanical impacts. Compos Part B Eng 152:209–219. https://doi.org/10.1016/J.COMPOSITESB.2018.07.004

35. Dong J, Locquet A, Citrin DS (2016) Enhanced Terahertz Imaging of Small Forced Delamination in Woven Glass Fibre-reinforced Composites with Wavelet De-noising. J Infrared, Millimeter, Terahertz Waves 37:289–301. https://doi.org/10.1007/s10762-015-0226-9

36. Serge Abrate (1998) Impact on composite structures. Cambridge university Press

37. Kim D-H, Ryu C-H, Park S-H, Kim H-S (2017) Nondestructive Evaluation of Hidden Damages in Glass Fiber Reinforced Plastic by Using the Terahertz Spectroscopy. Int J Precis Eng Manuf Technol 4:211–219. https://doi.org/10.1007/s40684-017-0026-x